Anomalous radar backscatter from Titan's surface?

M.A. Janssen [a,*], A. Le Gall [a], L.C. Wye [b]

[a] *Jet Propulsion Laboratory, California Institute of Technology, Pasadena, CA 91109, USA*
[b] *Stanford University, Electrical Engineering Department, Stanford, CA 94305, USA*

ABSTRACT

Since Cassini arrived at Saturn in 2004, its moon Titan has been thoroughly mapped by the RADAR instrument at 2-cm wavelength, in both active and passive modes. Some regions on Titan, including Xanadu and various bright hummocky bright terrains, contain surfaces that are among the most radar-bright encountered in the Solar System. This high brightness has been generally attributed to volume scattering processes in the inhomogeneous, low-loss medium expected for a cold, icy satellite surface. We can test this assumption now that the emissivity has been obtained from the concurrent radiometric measurements for nearly all the surface, with unprecedented accuracy (Janssen et al., and the Cassini RADAR Team [2009]. Icarus 200, 222–239). Kirchhoff's law of thermal radiation relates the radar and radiometric properties in a way that has never been fully exploited. In this paper we examine here how this law may be applied in this case to better understand the nature of Titan's radar-bright regions. We develop a quantitative model that, when compared to the observational data, allows us to conclude that either the reflective characteristics of the putative volume scattering subsurface must be highly constrained, or, more likely, organized structure on or in the surface is present that enhances the backscatter.

© 2010 Elsevier Inc. All rights reserved.

1. Introduction

To varying degree, the satellites of the outer planets show radar reflectivities that are large compared to other bodies in the Solar System (Campbell et al., 1977; Muhleman et al., 1990; Ostro et al., 2006). A generally accepted explanation is high-order volume scattering caused by inhomogeneities in a low-loss matrix such as water ice, made possible by the low microwave absorptivity of ice at cryogenic temperatures. Coherent backscattering such as from scatterers embedded in a weakly absorbing medium can explain both the large radar cross sections and unusual polarization ratios observed for the Galilean satellites using Earth-based radar (Hapke, 1990; Ostro, 1993; Black et al., 2001). Prior to Cassini's arrival at Saturn, Earth-based measurements of Titan showed a radar cross section that was small compared to the Galilean icy satellites (Muhleman et al., 1995), taken at the time to indicate more surface contaminants (Lorenz, 1998). However, the high spatial resolution achieved by the Cassini RADAR has revealed Titan's surface to be varied and complex, with many areas where the radar reflectivities in fact equal or exceed those of the most highly scattering icy satellites: Europa, Enceladus, and Tethys.

Radar reflectivity and thermal radiometry for any surface are related through Kirchhoff's law of thermal radiation, and the comparison of these quantities offers an approach to understanding the nature of planetary surfaces that is complementary to that using either radar or radiometry alone. There is a long history of using radar reflectivity and emissivity to study Earth, Moon, and Venus to date; however, little has been done to exploit Kirchhoff's law in any quantitative sense, largely because of the paucity of relevant data, uncertainties inherent in their interpretation, and the typically much lower spatial resolution of radiometry compared to radar. De Pater et al. (1984) compared the Galilean satellite brightness temperatures obtained from VLA measurements to radar albedos using a simplified model based on Kirchhoff's law, noting the general consistency of the derived physical surface temperatures with those obtained by other means. Muhleman et al. (1995) noted the inverse relationship between radar cross section and disk brightness temperature for the Galilean satellites and Titan, although without comment on the quantitative nature of this relationship. More recently Ostro et al. (2006) demonstrated this relationship in a plot of radar albedo vs. emissivity using disk-averaged passive and active observations of the saturnian satellites obtained by the Cassini RADAR, again without quantitative analysis. In this paper we take advantage of the extensive and uniquely calibrated radiometric observations of Titan obtained concurrently with the radar mappings at closest approach to quantitatively examine how comparison of these quantities can contribute to understanding the nature of Titan's surface, particularly its radar-bright regions.

In Section 2 we develop a model that describes the relationship of radar backscatter to emissivity for the case of backscatter measured in a single linear polarization, as applies for the Cassini

* Corresponding author. Fax: +1 818 354 8895.
E-mail addresses: michael.a.janssen@jpl.nasa.gov (M.A. Janssen), alice.le-gall@jpl.nasa.gov (A. Le Gall), lcwye@stanford.edu (L.C. Wye).

RADAR. This combined emission-backscatter (CEB) model presumes a diffuse volume scattering medium such as might be expected for a cold, low-loss icy surface, generalized to include polarization, coherent backscattering, and a possible specular component. Following this, in Section 3, we describe the observational data on Titan for radiometry and radar reflectivity. In Section 4 we compare the model to observations and draw conclusions about the applicability of the CEB model and possible surface characteristics. We discuss implications for Titan's radar-bright regions in the concluding section.

2. Theoretical background

2.1. Kirchhoff's law of thermal radiation

The emissivity of a surface is complementary to its reflectivity as expressed by Kirchhoff's law of thermal radiation. With radar applications specifically in mind, Peake (1959) (see also Ulaby et al. (1981, 1982)) derived an expression for Kirchhoff's law for a general nonuniform surface that relates the emissivity of the surface to its bistatic radar scattering coefficients. In particular consider the albedo A_p, the fraction of power that is scattered from an element of surface due to a wave of polarization p incident from a vertical angle θ and azimuth ϕ which may be expressed in conventional radar terminology as

$$A_p(\theta, \phi) = \frac{1}{4\pi} \iint_{upper\ hemisphere} \left[\frac{\sigma_{pp}^0(\theta, \phi; \theta_s, \phi_s) + \sigma_{pq}^0(\theta, \phi; \theta_s, \phi_s)}{\cos \theta} \right] d\Omega_s \quad (1)$$

where σ_{pp}^0 and σ_{pq}^0 are the bistatic coefficients for the scattering of the incident wave into the direction θ_s, ϕ_s in respective orthogonal polarizations p and q, and $d\Omega_s = \sin \theta_s\, d\theta_s\, d\phi_s$ is the solid angle in the scattering direction θ_s, ϕ_s. Peake showed that the emissivity $e_p(\theta, \phi)$ viewed from the same direction and at the same polarization is the complement of this albedo, or

$$e_p(\theta, \phi) = 1 - A_p(\theta, \phi) \quad (2)$$

No restrictions are placed on the surface other than that it is contained in a half space in which the reflection back into the free-space hemisphere can occur by any combination of absorption, surface and volume scattering. In particular, it is not restricted to surfaces satisfying the Kirchhoff approximation (cf. Kang et al., 1985).

2.2. Relating backscatter to emissivity

In practice, bistatic scattering coefficients are rarely obtained, and never fully. Most investigations, including the present, depend on monostatic observations in which only the backscattering cross section is measured and, as in our case, in only one polarization. As a consequence, we must make assumptions about how the backscattering relates to the hemispherical scattering properties of the surface in order to make use of this relationship. Concerning the emissivity, in the case of Titan's surface as observed by the Cassini RADAR, the absolute radiometric calibration is known and the surface temperature distribution is independently determined from other Cassini and Huygens probe measurements; consequently, the emissivity can be well estimated (Janssen et al., 2009).

In this section we develop a simple but reasonably general model to explore the relationship between the measured emissivities and backscatter for the most radar-bright regions on Titan. We begin by considering an idealized diffuse scattering surface, which allows us to integrate Eq. (1) and obtain a simple expression for the Kirchhoff relationship in Eq. (2). Since the Cassini instrument measures same-sense linear polarization only, we specialize to linear

polarization for this and the following. We then incorporate a small quasispecular component to the reflection and modify the expression for the Kirchhoff relationship accordingly.

The diffuse component of the reflection from many surfaces encountered in the Solar System can be described by a $\cos^n$ scattering law. In our case the approximate monostatic scattering law takes the form

$$\sigma_{pp}^0(\theta, \phi; \theta, \phi) \equiv \sigma_{pp}^0\ (\text{backscatter}) = \sigma(0) \cos^n \theta \quad (3)$$

where the incident and reflected waves are measured in same-sense linear polarization, and $\sigma(0)$ is the diffuse scattering coefficient at normal incidence. Typically $1 \leqslant n \leqslant 2$, where the limiting cases $n = 1$ and $n = 2$ describe isotropic and Lambertian scattering surfaces respectively (cf. Ulaby et al., 1981, 1982). Let us outline a simple model that follows this law and at the same time allows an analytical solution for the albedo in Eq. (2). In particular, let us write the sum of the bistatic scattering coefficients as

$$\sigma_{pp}^0\ (\theta, \phi; \theta_s, \phi_s) + \sigma_{pq}^0\ (\theta, \phi; \theta_s, \phi_s) = (1 + \mu_L(\theta, \phi))\, \sigma(0) \cos^{n-1} \theta_s \cos \theta \quad (4)$$

where the linear polarization ratio $\mu_L = \sigma_{pq}^0 (\text{backscatter})/\sigma_{pp}^0$ (backscatter) and for a general surface may be a function of θ and ϕ. This expression describes the total power reflected from a surface element dA, on which the illumination is proportional to $\cos \theta$, distributed into the visible hemisphere with power proportional to $\cos^{n-1} \theta$—without further restriction on the distribution of power between polarizations over the hemisphere. In particular, it reduces to the form of Eq. (3) in the backscattering direction ($\theta_s = \theta$, $\phi_s = \phi + \pi$) if μ_L is constant. This expression covers diffuse reflection without regard to its source (i.e., from the surface or subsurface) and the quasispecular component of the reflection, if any, must be handled separately. After substitution into Eq. (1) we may carry out the integration to obtain from Eq. (2)

$$e_p(\theta, \phi) = e_p = 1 - \frac{1 + \mu_L(\theta, \phi)}{2n} \sigma \quad (5)$$

Using the expression for the backscattering in Eq. (3), we arrive at the basic model expression

$$e_p = 1 - \left(\frac{1 + \mu_L}{2n} \right) \frac{\sigma_{pp}^0(\text{backscatter})}{\cos^n \theta} \quad (6)$$

where we drop the explicit notation of viewing geometry dependence on μ_L. Note from Eq. (5) that the emissivity is a function of only the model parameters μ_L, n, and $\sigma(0)$, where at least n and $\sigma(0)$ are constant. If μ_L is also constant the emissivity will be independent of emission angle and the observed polarization—such a surface would display unpolarized thermal emission that is constant with emission angle.

This model approximately describes an important class of complex surfaces. Volume scattering from an inhomogeneous subsurface is of particular interest for Titan as well as for other ice-mantled satellites in the outer Solar System because of the low dielectric loss typical for ices at cryogenic temperatures and the correspondingly long penetration lengths and increased opportunities for scattering. Such conditions can be expected to lead to the strong diffuse scattering component observed on Titan (e.g., Zebker et al., 2008). In the backscatter direction, we must further consider the possibility of coherent backscattering. Here photons that are multiply scattered in a weakly absorbing medium and traverse the same path in opposite directions can combine coherently in the backscatter direction to produce an increased intensity (Hapke, 1990). In the limit of low loss, this increase can be as much as a factor of two higher than the cross section in nearby directions, where the angular width of the scattering enhancement depends

on details of the medium such as mean scattering length. If coherent backscattering is considered, then we may modify Eq. (6) as

$$e_p = 1 - \left(\frac{1 + \mu_L}{2f_{cbe}n}\right)\frac{\sigma^0_{pp}(\text{backscatter})}{\cos^n \theta} \qquad (7)$$

where $1 \leqslant f_{cbe} \leqslant 2$ accounts for the possible coherent backscattering effect (CBE). This addition to the model is an approximation since we ignore the contribution to the albedo in Eq. (1) due to the scattering enhancement around the backscatter direction. Since this is typically of small angular width, however, this approximation is expected to be of negligible significance.

So far we have neglected the possibility of a quasispecular surface reflection. The low emissivities compared to low thermal polarizations in Titan's radar-bright regions allow us to conclude that volume scattering is the dominant mechanism of reflection in these regions (Janssen et al., 2009); nevertheless, let us consider a small component of quasispecular reflection $\sigma^0_{pp}(\theta, \phi; \theta_s, \phi_s)$ added to the purely diffuse scattering model considered above. Since these two mechanisms are independent, the total observed backscatter can be written as

$$\sigma^0_{pp\,total}\,(\text{backscatter}) = \sigma(0)\cos^n \theta + \sigma^0_{p_{qs}}\,(\text{backscatter}) \qquad (8)$$

The bistatic quasispecular component will in general depend on angle and polarization, although a surface with only moderate roughness will tend to retain the polarization of the linearly polarized incident wave. We assume a simplified model here in which the linear polarization is retained. In particular we include $\sigma^0_{p_{qs}}(\theta, \phi; \theta_s, \phi_s)$ in the integrand of Eq. (1) to obtain the quasispecular albedo contribution $A_{p_{qs}}(\theta, \phi)$, which then leads to the result for the emissivity

$$e_p(\theta, \phi) = 1 - \left(\frac{1 + \mu_L}{2f_{cbe}n}\right)\frac{\sigma^0_{pp\,diffuse}(\text{backscatter})}{\cos^n\theta} - A_{p_{qs}}(\theta, \phi) \qquad (9)$$

In this formulation $\sigma^0_{pp\,diffuse}$ denotes just the diffuse backscattering component. This expression then describes our final combined emission-backscatter (CEB) model. The quasispecular albedo $A_{p_{qs}}$ may be estimated from the observed backscattering dependence on incidence angle near normal incidence. We model the near-nadir backscatter response with traditional quasispecular scattering laws and use the retrieved dielectric constant values to estimate the full Fresnel reflection coefficients. The Fresnel reflection coefficients describe the total power scattered from a single reflection off a smooth surface at a given polarization and incidence angle. We approximate the total reflected quasispecular power integrated over all directions $A_{p_{qs}}$ by the total power scattered from a single reflection from the smooth mean surface as given by the appropriate smooth-surface Fresnel reflection coefficient.

3. Observations

Titan's surface has been observed extensively at 2-cm wavelength by the Cassini RADAR instrument, in scatterometery and altimetry modes as well in the high-resolution synthetic aperture radar (SAR) mode (Elachi et al., 2004; Lunine et al., 2008; Wye et al., 2007). Radiometric data at the same wavelength have been obtained concurrently in all Radar modes (Janssen et al., 2009). The radiometric data were absolutely calibrated based on the surface temperature measurement by the Huygens probe and interpretation of radiometry collected on the northern seas and dunes fields, as described by Janssen et al. (2009). Polarized radiometry was used to construct a global map of effective dielectric constant, the use of which allowed the construction of a global map of the equivalent brightness temperature at normal incidence to an accuracy approaching 1 K. The published maps were based on all Titan data collected through the T30 pass in May 2007, and we have

subsequently extended these maps using the additional data obtained through the T65 pass in January 2010.

The radiometry map was used to obtain a map of emissivity at normal incidence using a model for Titan's surface temperature. The Huygens probe measurement was extended globally based on an equator-to-pole gradient of about 2 K inferred from measurements of atmospheric temperature near the surface by CIRS (Jennings et al., 2009) and occultation observations obtained by the Radio Science experiment (Schinder et al., 2008). Other temperature variations are expected to be small (~1 K) because of the atmosphere's large thermal inertia, Titan's modest topographical variations (Stiles et al., 2009), and expected small diurnal variations (e.g., Lorenz et al., 2003; Janssen et al., 2009). The resulting map of emissivity is estimated to be accurate to about 2%.

The radar reflectivity of Titan's surface has been measured in both real aperture (scatterometry) and synthetic aperture (SAR) mode. Both approaches are valuable for this study. The radiometry in SAR mode has the highest spatial resolution (approaching 6 km) and hence the best ability to discriminate among diverse terrains (Paganelli et al., 2007); further, the incidence angles used in SAR mode are only 10–30° removed from nadir where the emissivity is best determined. The scatterometry on the other hand covers the full range of incidence angle, which is important to determine the monostatic scattering laws for various terrains (Wye et al., 2007, 2008) and to look for the presence of a quasispecular component. The radar data have been calibrated to about 1.3 dB, or 35%, quoted at the 3-σ level by West et al. (2009). For purposes of comparing active with passive measurements we use the 1-σ value of 12% for this error, applicable for both SAR and scatterometry.

4. Discussion

We first examine the relationship between active and passive measurements in SAR mode, comparing the radiometric brightness observed in the real-aperture beam footprint with the averaged value of σ^0 over the same footprint, using the measured beam pattern for the averaging. While SAR maps are typically "corrected" to normal incidence values using an assumed scattering law, we use the calibrated but "uncorrected" value here. Although the radiometry is taken at the same incidence angle as the concurrent SAR data, the radiometric calibration process to remove the strong sidelobe contribution at close range to Titan results in brightness temperatures that are strictly referenced to their equivalent values at normal incidence. Hence it is necessary to adjust the calibrated values back to the actual emission angle of the observation, which we accomplish using the dielectric map and a model for the emission angle dependence of the brightness (White and Cogdell, 1973). For the terrains examined here and the typical range of incidence angles used in SAR mapping (10–30°) the correction is less than 1 K, however, so that errors in this adjustment do not contribute significantly to the net uncertainty in the derived emissivity.

Fig. 1 shows the relationship between the emissivities thus obtained in SAR mode and the concurrently obtained averaged values of σ^0 for selected regions on Titan's surface. These regions are placed in geographical context in Fig. 2 and include the bright core of Xanadu, hummocky bright terrains outside of Xanadu, dunes and radar-gray regions (which are what Lopes et al. (2010) classified as *undifferentiated plains*) seen in SAR swaths obtained during the T13 (Xanadu core), T3 (hummocky terrains), T21 (hummocky and radar-gray terrains), T41 (radar-gray terrains), and T43 (dunes and Xanadu core) flybys. Xanadu is of special interest in this work, particularly its core, which we identify in Fig. 3 as its most radar-bright and least emissive region. Regions outside of the radar-bright terrains of Xanadu and the hummocky mountains are presented to show that a much different correlation is seen
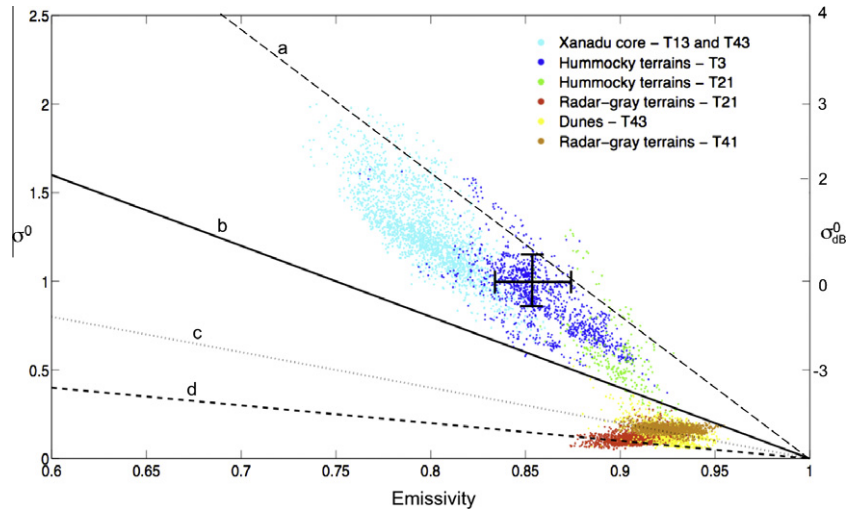
Fig. 1. Scatter plot of emissivity vs. σ^0 for selected regions on Titan, with emissivity obtained as described in the text and σ^0 uncorrected for incidence angle (see Fig. 2 for location). The terrains include radar-bright regions within and outside Xanadu as well as others that show much different behavior. Representative CEB model curves are shown in which we assume $\theta = 0$ and no quasispecular contribution ($A_{P_{qs}} = 0$) to provide the maximum value of diffuse σ^0 for each emissivity. Specifically, we have (curve a), the extreme maximum case for a given emissivity consisting of a Lambertian surface ($n = 2$) with maximum coherent backscattering ($f_{cbe} = 2$) and full conservation of same-sense linear polarization ($\mu_L = 0$); (curve b) $n = 2$ and midrange values for μ_L and f_{cbe} ($\mu_L = 0.5$ and $f_{cbe} = 1.5$); (curve c) $n = 2$ with unpolarized reflection and no coherent backscattering ($\mu_L = 1$ and $f_{cbe} = 1$); and (curve d) the extreme minimum case including an isotropically scattering surface ($n = 1$) with $\mu_L = 1$ and $f_{cbe} = 1$. The uncertainties in emissivity and radar cross section are indicated for a representative point. The left-hand vertical scale shows the backscattering coefficient σ^0 on a linear scale, while the right-hand scale shows the commonly used logarithmic equivalent.
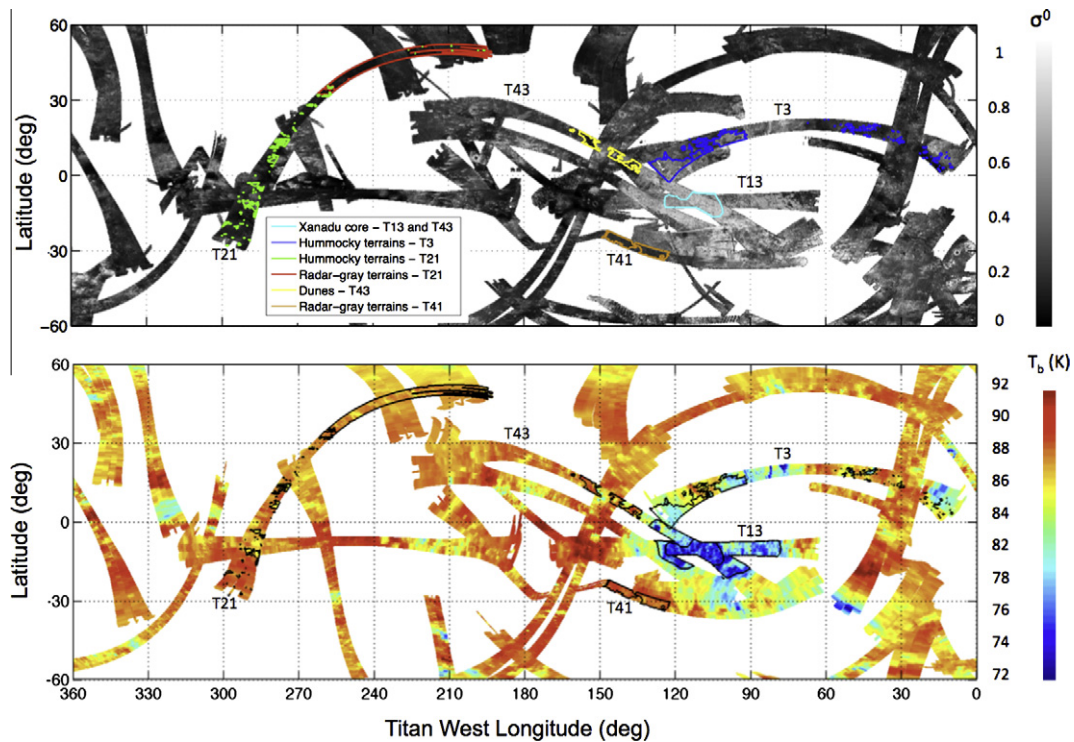

Fig. 2. Location of selected regions used in the scatter plot of Fig. 1. The top panel shows a map of all values of σ^0 obtained in SAR mode through the prime mission. Regions examined in this paper are indicated by the colored boundaries using the same color code as for the points plotted in Fig. 1. The bottom panel shows the corresponding map of radiometric brightness temperature.

between the radiometry and the radar cross sections over the rest of Titan—the latter remain to be studied and will not be considered further here. The model curves shown in Fig. 1 are CEB models for purely diffuse scattering (i.e., the quasispecular albedo $A_{P_{qs}} = 0$) in which the parameters n, μ_L, and f_{cbe} are chosen to illustrate the range of possibilities. The distribution of the observed emissivities in the bright terrains show an approximately linear relationship

with σ^0 as predicted by the modeling, but with only parameters tending toward the extreme case ($n = 2$, $\mu_L = 0$, and $f_{cbe} = 2$) able to match the slope.

In general we must take into account the angular dependences of the measured backscatter and emissivity for comparison with the models. As a first step we examined the emission angle dependence of the emissivity in Xanadu and its core. Fig. 4 shows plots of
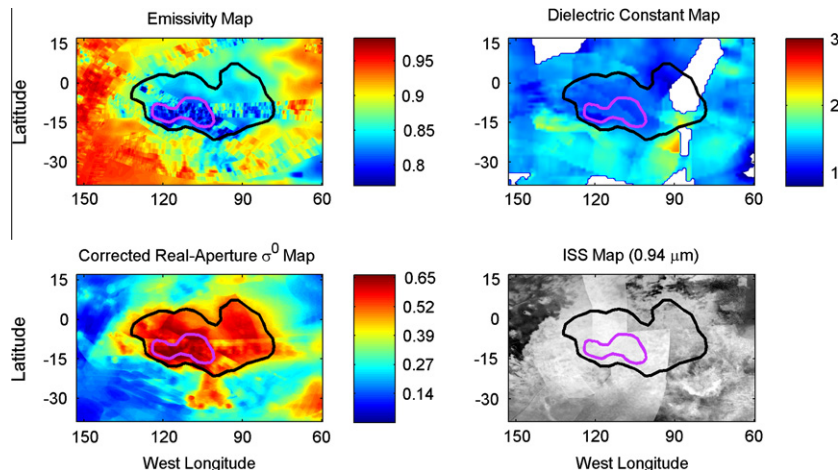
Fig. 3. Maps of Xanadu observed by the RADAR radiometer as emissivity at normal incidence (upper left panel), dielectric constant (upper right panel), the Radar in real-aperture mode (lower left panel), and the Imaging Science Subsystem (ISS) instrument at near-infrared wavelengths (lower right panel). The black boundary depicts Xanadu, while the inner, purple boundary defines what we call the Xanadu core for the purposes of this paper. The two boundaries are chosen by following the joint contours in the radiometry and real-aperture radar maps.
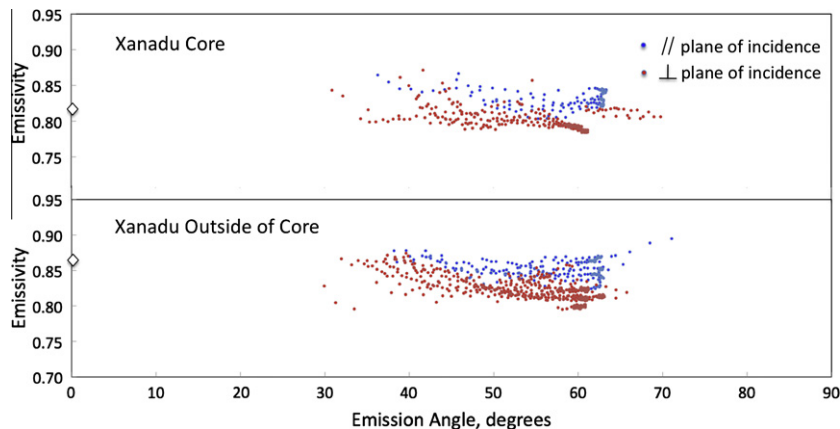

Fig. 4. Emissivity of the Xanadu core as a function of emission angle as determined from accumulated radiometric measurements. The colored points identify the dominant polarization: red, within 30° of parallel to the plane of incidence (V), and blue, within 30° of the perpendicular to the plane of incidence (H). The small differences are consistent with a surface of effective dielectric constant of about 1.3.

brightness temperature vs. emission angle collected from all brightness temperature measurements that resolve Xanadu and its core and require minimum correction for the contribution from the disk of Titan seen in the beam sidelobes. The Xanadu core and the remainder of Xanadu are examined separately and shown in the two respective panels. Because we want to examine the emission angle dependence explicitly, we must correct individual measurements for the sidelobe contamination rather than use the map-making process described above that yields normal incidence maps. We used the far sidelobe model obtained in Janssen et al. (2009) to accomplish this, selecting only data obtained from ranges outside of 10,000 km where the uncertainty in the sidelobe correction is less than about 2 K. We further sorted the data by polarization, assigning observations made with polarization angles within 30° of perpendicular or parallel to the plane of incidence to the respective H and V polarizations. The average emissivity at normal incidence is shown by the diamond along the ordinate in each panel. While some residual systematic errors are apparent, the net results show little or no emission angle dependence from normal incidence to 70° in all cases, consistent with the CEB model and a value of μ_L that is independent of viewing geometry. In particular

the small (~0.02) emissivity difference between the H and V polarizations in each panel is consistent with the small dielectric constant 1.2–1.4 obtained from the polarization map for the Xanadu core (Fig. 3, upper left panel), and is consistent with the presence (if not magnitude, see below) of a small quasispecular component.

All of the active radar data (SAR, scatterometry, and altimetry) collected from Xanadu and the bright hummocky terrains were then examined to obtain the angular dependence of the measured backscatter as well as to look for evidence of a surface reflection that could possibly explain the high backscatter observed. These data are all calibrated and processed in the same real-aperture sense (e.g., see above and Wye et al. (2007, 2008)) and use a self-consistent calibration procedure. Fig. 5 shows all such real-aperture measurements of σ^0 obtained on Xanadu's core, the remainder of Xanadu, and the hummocky terrains, grouped into regions. The left-hand panels describe the fit of an empirical scatterometry model to the respective data sets as discussed next, while the right-hand panels compare the CEB model to the same data, discussed following.

The light blue points in the upper left-hand panel represent the real-aperture SAR values obtained in the T13 and T43 passes in the
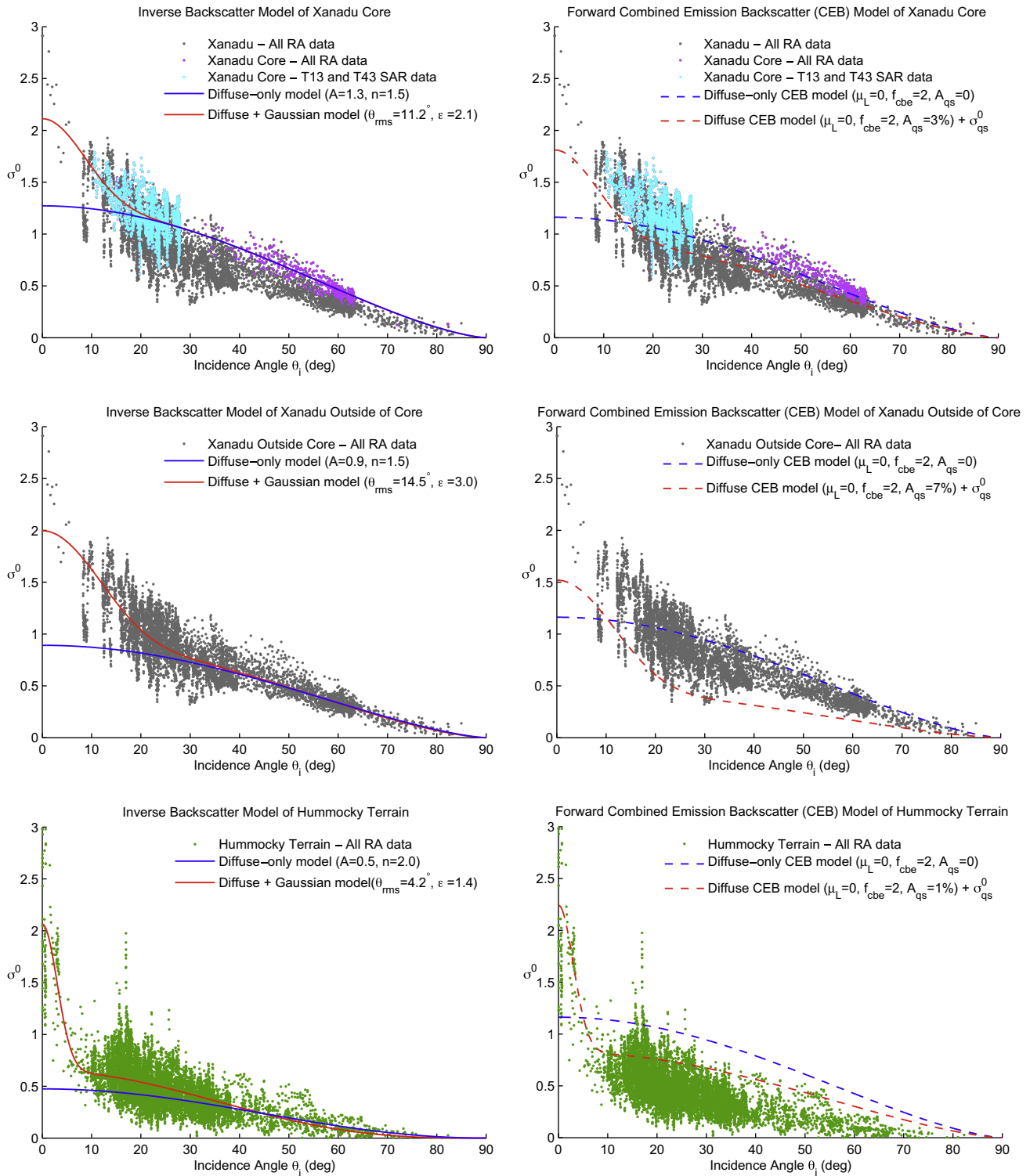
Fig. 5. Incidence angle dependence of σ^0 for Xanadu and hummocky bright terrains. The terrains are considered in three groupings, the Xanadu core (upper panels), Xanadu outside of the core (middle panels), and the hummocky terrains (lower panels). The Xanadu core is the most radar-bright region on Titan, which we consider separately from the remainder of Xanadu, with the respective boundaries defined in Fig. 3. The left-hand panels show accumulated real aperture data for these terrains, with fits to the data (inverse backscattering models) using the composite scattering law described in the text (blue solid curves, diffuse component $A \cos^n \theta$ only; red solid curves, Gaussian quasispecular plus diffuse component). The right-hand panels show the predictions of the CEB model (forward models) for the retrieved parameters n and A_{qs} obtained from the inverse fits assuming extreme values $\mu_L = 0$ and $f_{cbe} = 2$, and considering the diffuse component only (dashed blue curves) and Gaussian quasispecular plus diffuse component (dashed red curves).

Xanadu core, while the remainder represent real-aperture observations collected in the other active modes (scatterometry and altimetry) throughout Xanadu (gray) and in the core only (purple). The

middle left-hand panel shows the data collected in Xanadu outside the core, and the lower panel shows the data collected in the hummocky bright terrains. Following the modeling procedure of Wye

et al. (2007), the solid curves in each of the left-hand panels show the results of empirical fits to the respective data sets using a composite scattering law that is the sum of a diffuse component modeled with an $A \cos^n \theta$ dependence and a quasispecular component that we find is best modeled with the traditional Gaussian backscatter law

$$\sigma_G^0 = \frac{\rho C}{\cos^4 \theta} \exp\left(-C \tan^2 \theta\right) \qquad (10)$$

where $\rho = \left(\frac{\sqrt{\varepsilon} - 1}{\sqrt{\varepsilon} + 1}\right)$ and $C = 1/\tan^2 \theta_{rms}$.

For example, the Xanadu core data are best described with values $A = 1.27$ and $n = 1.45$ for the diffuse term, and rms slope $\theta_{rms} = 11.2°$ and dielectric constant $\varepsilon = 2.1$ for the quasispecular term. The solid blue curve is the diffuse component fit alone, while the solid red curve is the composite fit. Using other common quasispecular laws, such as Hagfors' law or an exponential scattering law, or combinations of the various laws, would negligibly affect our results and conclusions for all the terrains depicted. In fact, we find that the Gaussian law typically yields lower dielectric constant estimates than the other laws, thus tending towards a lower bound on $A_{P_{qs}}$ and subsequently an upper bound on the CEB backscatter.

The Xanadu core data are plotted again in the upper right-hand panel, where the dashed curves show values for the CEB model using (1) the average emissivity for the core at normal incidence, taken to be independent of emission angle as justified by the results shown in Fig. 4, (2) parameters for the quasispecular component found from the above analysis and (3) extreme values $\mu_L = 0$ and $f_{cbe} = 2$. In particular we solve Eq. (9) for $\sigma_{pp\,diffuse}^0$, using the single Fresnel reflection approximation for $A_{P_{qs}}$, assuming perpendicular polarization (the polarization used for SAR data collection) where the dielectric constant is set to the values retrieved from the quasispecular model. We add the quasispecular backscatter σ_G^0 modeled by Eq. (10) to $\sigma_{pp\,diffuse}^0$ to obtain the curves shown. We note that the presence of the quasispecular component generally reduces the backscatter at large angles. In effect, the observed emissivity constrains the amount of reflectivity into the upper hemisphere, and if that total reflectivity includes quasispecular surface scatter (or any vertically enhanced backscatter whatever the cause), then less power is available to explain the diffuse scattering levels away from the specular reflection.

We see that the extreme CEB model provides only a marginal fit to the Xanadu core data, although perhaps within range if we allow radar calibration errors exceeding the one-sigma level. The remainder of the Xanadu data are poorly fit even with the extreme version of the diffuse CEB model (middle right panel) because of the apparent presence of a strong quasispecular component. On the other hand the hummocky terrain appears to be easily within reach of the CEB model (lower right panel).

The CEB model thus provides a possible fit, although tightly constrained, to the observations for the Xanadu core; namely, the surface must perfectly preserve the incident linear polarization while the coherent backscattering is at its maximum. Many natural surfaces have been shown to demonstrate small values for μ_L, sometimes even approaching zero (e.g., rain forests in which double-bounces from tree trunks to wet ground dominate the reflection, Rignot, 1995). On the other hand it is not clear that a surface such as Xanadu that absorbs at least 70% of all incident radiation can produce a coherent backscattering enhancement approaching $f_{cbe} = 2$. The fit with emission angle might be improved by allowing μ_L to vary, but at the expense of increasing the amplitude discrepancy.

How general is this model? For the diffuse component as given in Eq. (4) the angular dependence of the reflected power per unit surface area (i.e., the bistatic cross section) from a given incidence angle is assumed to be the same as the angular dependence of the measured backscatter per unit surface area (the monostatic cross section). While this is a reasonable assumption for high-order multiple scattering in a low-loss subsurface, it is not necessarily a general property of surfaces; e.g., it is not true for the quasispecular component of the reflection (and may not be true for the diffuse component of a surface reflection, although this is expected to be small in our case and we have subsumed it into the diffuse component of our CEB model). Nevertheless some model is required to infer the bistatic scattering distribution into the visible hemisphere based on our measurement of the backscattering. If, for example, the bistatic cross section for the scattering of total power were to decrease away from the angle of incidence faster than the measured backscatter response would suggest, then the CEB model would overestimate the reflectivity and hence underestimate the emissivity for that angle of incidence. This could possibly happen if μ_L were allowed to vary with incidence angle, but then the emissivity would vary as well. There is no evidence this, however, which implies that whatever peculiarity may exist in the bistatic scattering coefficient for Xanadu at a given angle must be the same at other incidence angles. In particular, the measured backscatter appears to consistently overpredict the surface reflectivity at all incidence angles; i.e., the backscattering is enhanced by some process not included in the CEB model.

We suggest that this enhancement may be due to some wavelength-scale organized structure on the surface analogous to reflective paint or pearlescent coatings for movie screen at visible wavelengths. Even the quasispecular peak seen in the upper right panel of Fig. 5 could be due to a vertically focused backscattering element on the surface unrelated to an actual specular component, which for example might explain the discrepancy between the relative quasispecular power in the backscattering from the Xanadu core ($\sim$3%) and that predicted from the polarized thermal emission (0.2%). The much stronger apparent quasispecular power seen in the rest of Xanadu ($\sim$7%, middle right panel of Fig. 5) may be a clue. If this were truly due to surface reflection, specular emission models for moderately rough surfaces indicate that the polarization of the thermal emission should be well in excess of that actually seen (Janssen et al., 2009), providing a stronger argument for vertically focused backscattering instead of quasispecular reflection.

The apparent discrepancies between backscatter and emissivity could possibly be accounted for by underestimated errors in emissivity ($\pm$0.02) and σ^0 ($\pm$12%). The uncertainty in emissivity is well bounded by observation as discussed in Janssen et al. (2009). Radar calibrations are more difficult to verify and depend on knowledge of transmitter power, receiver path losses, receiver gain, and beam solid angle. West et al. (2009), describe validation of receiver path losses and receiver gain by observation of thermal power from Saturn in the radar receiver band, while the determination of beam solid angle and power loss through sidelobes is based on thorough radiometric measurements using the instrument's radiometer channel (Mizzoni, 2006; Janssen et al., 2009). The transmitter power was measured prior to launch at 48 W. This power would have to have somehow doubled to explain the discrepancy, which we consider unlikely.

5. Conclusions

Many models can explain the observed strong backscattering on icy satellites; however, we have shown that concurrent radiometry places a significant constraint on the magnitude of this backscattering. In the case of at least some of the radar-bright regions in Xanadu, no plausible high-order random-scattering process such as studied by Black et al. (2001) appears capable of explaining

the observed backscattering in a way that is consistent with the relatively modest decrease seen in emissivity, even if such a surface can be shown to both preserve incident linear polarization while providing the maximum coherent backscatter.

As an alternative we suggest the presence of ordered structure on or within the surface that enhances backscatter. There are many theoretical possibilities for such an enhancement, for example a layer of corner cube reflectors, while the challenge is to select those that are geologically plausible. For example, Le Gall et al. (2010) have examined a possibility that can explain the otherwise puzzling radar-bright channels seen in many regions of Titan, proposing that the enhanced backscatter is due to layers of rounded ice "river rocks" created by fluvial processes. While this is an unlikely explanation for rough terrain in Xanadu not otherwise associated with flows, such surface structures are likely, with implications for the geology of these regions. Goldstein and Green (1980) have shown that low-loss fractured ice can explain the unusual polarization ratios observed for some icy satellites, although it remains to be shown that such a model can both preserve linear polarization and produce coherent backscatter. Hagfors et al. (1997) have discussed generic processes based on refractive scattering that can result in the unusual polarizations observed in icy satellites while allowing a radar cross section that is enhanced beyond the coherent backscattering model. As an example, they note the unusual cross sections seen in the percolation zone of the Greenland ice sheet, modeled as due to ice cylinders (Rignot et al., 1993; Rignot, 1995). A systematic ordering of fracturing such as that seen to occur in some types of cooled surficial lava flows on Earth that produce columnar basalts may occur following water flows on Titan, leading to cylindrical structures that could behave like those in the Greenland ice sheet (Rignot, 1995). Deposits of solutes carried to the surface by capillary action of liquid can form pinnacles such as seen in the exposed salt beds of the Devil's Golf Course in Death Valley, California. Such structure could be produced by organic solutes in methane evaporating from Titan's surface. Pinnacles, as well as cylinders or oblate spheroids amenable to non-random orientation on the surface, could produce the kind of vertically focused backscatter suggested for Xanadu, particularly in the region outside its core.

Finally, the interpretation of the data presented here is limited by the lack of information on the polarization properties of the radar return signal. Radar polarimetry is a well-known technique used in Earth-based applications (cf. Ulaby and Elachi, 1990). The present analysis indicates that this is a powerful approach for the investigation of icy satellite surface properties and is recommended for subsequent missions to the outer planets.

Acknowledgments

References

Black, G.J., Campbell, D.B., Nicholson, P.D., 2001. Icy Galilean satellites: Modeling radar reflectivities as a coherent backscattering effect. Icarus 151, 167–180.

Campbell, D.B., Chandler, J.F., Ostro, S.J., Pettengill, G.H., Shapiro, I.I., 1977. Galilean satellites: 1976 Results. Icarus 34, 254–267.

De Pater, I., Brown, R.A., Dickel, J.R., 1984. VLA observations of the Galilean satellites. Icarus 57, 93–101.

Elachi, C. et al., 2004. RADAR: The Cassini Titan radar mapper. Space Sci. Rev. 115, 71–110.

Goldstein, R.M., Green, R.R., 1980. Ganymede: Radar surface characteristics. Science 207, 179–180.

Hagfors, T., Dahlstrom, I., Gold, T., Hamran, S.-E., Hansen, R., 1997. Refraction scattering in the anomalous reflections from icy surfaces. Icarus 130, 313–322.

Hapke, B., 1990. Coherent backscatter and the radar characteristics of outer planet satellites. Icarus 88, 407–417.

Janssen, M.A. et al., and the Cassini RADAR Team, 2009. Titan's surface at 2.2-cm wavelength imaged by the Cassini RADAR radiometer: Calibration and first results. Icarus 200, 222–239.

Jennings, D.E. et al., 2009. Titan surface brightness temperatures. Astrophys. J. 691, L103–L105.

Kang, L.T., Kong, J.A., Shin, R.T., 1985. Theory of Microwave Remote Sensing. John Wiley & Sons, New York.

Le Gall, A., Janssen, M.A., Paillou, P., Lorenz, R.D., and the Cassini RADAR Team, 2010. Radar-bright channels on Titan. Icarus 207, 948–958.

Lopes, R.M.C. et al., and the Cassini RADAR Team, 2010. Distribution and interplay of geologic processes on Titan from Cassini RADAR data. Icarus, 205, 540–558.

Lorenz, R.D., 1998. Preliminary measurements of the cryogenic dielectric properties of water–ammonia ices: Application to radar observations of icy satellites. Icarus 136, 344–348.

Lorenz, R.D., Builloz, G., Encrenaz, P., Janssen, M.A., West, R.D., Muhleman, D.O., 2003. Cassini RADAR: Prospects for Titan surface investigations using the microwave radiometer. Planet. Space Sci. 51, 353–364.

Lunine, J.I. et al., 2008. Titan's diverse landscapes as evidenced by Cassini RADAR's third and fourth looks at Titan. Icarus 195, 415–433.

Mizzoni, R., 2006. The Cassini high-gain antenna subsystem. In: Imbriale, W.A. (Ed.), Spaceborne Antennas for Planetary Exploration, Deep Space Communication and Navigation Series. Jet Propulsion Laboratory, pp. 257–303.

Muhleman, D., Grossman, A., Butler, B., Slade, M., 1990. Radar reflectivity of Titan. Science 248, 975–980.

Muhleman, D.O., Grossman, A.W., Butler, B.J., 1995. Radar investigation of Mars, Mercury, and Titan. Annu. Rev. Earth Planet. Sci. 23, 337–374.

Ostro, S.J., 1993. Planetary radar astronomy. Rev. Mod. Phys. 65, 1235–1279.

Ostro, S.J. et al., and the Cassini RADAR Team, 2006. Cassini RADAR observations of Enceladus, Tethys, Dione, Rhea, Iapetus, Hyperion, and Phoebe. Icarus 183, 479–490.

Paganelli, F. et al., and the Cassini RADAR Team, 2007. Titan's surface from the Cassini RADAR SAR and high resolution radiometry data of the first five flybys. Icarus 191, 211–222.

Peake, W.H., 1959. Interaction of electromagnetic waves with some natural surfaces. IRE Trans. Antennas Propagation V-7, S324–S329.

Rignot, E., 1995. Backscatter model for the unusual radar properties of the Greenland ice sheet. J. Geophys. Res. 100 (E5), 9389–9400.

Rignot, E., Ostro, S.J., Van Zyl, J.J., Jezek, K.C., 1993. Unusual radar echoes from the Greenland ice sheet. Science 261, 1710–1713.

Schinder, P.J., Flasar, F.M., Marouf, E.A., French, R.G., McGhee, C.A., Kliore, A.J., Rappaport, N.J., 2008. The structure of the atmosphere of Saturn at Mid-latitudes from Cassini Radio Occultations. Bull. Am. Astron. Soc. 40, 475.

Stiles, B.W. et al., and the Cassini RADAR Team, 2009. Determining Titan surface topography from Cassini SAR data. Icarus, 202, 584–598.

Ulaby, F.T., Elachi, C., 1990. Radar Polarimetry for Geoscience Applications. Artech House, Norwood, Mass.

Ulaby, F.T., Moore, R.K., Fung, Adrian K., 1981. Microwave Remote Sensing, Active and Passive. Microwave Remote Sensing Fundamentals and Radiometry, vol. I. Addison-Wesley, Reading, Mass.

Ulaby, F.T., Moore, R.K., Fung, Adrian K., 1982. Microwave Remote Sensing, Active and Passive. Radar Remote Sensing and Surface Scattering and Emission Theory, vol. II. Addison-Wesley, Reading, Mass.

West, R. et al., 2009. Cassini RADAR sequence planning and instrument performance. IEEE Trans. Geosci. Remote Sensing 47 (6), 1777–1795.

White, T.L., Cogdell, J.R., 1973. Lunar polarization studies at 3.1 mm wavelength. Moon 6, 235–249. doi:10.1007/BF00562205.

Wye, L.C. Zebker, H.A., Ostro, S.J., West, R.D., Gim, Y., Lorenz, R.D., and the Cassini RADAR Team, 2007. Electrical properties of Titan's surface from Cassini RADAR scatterometer measurements. Icarus 188, 367–385.

Wye, L.C., Zebker, H.A., West, R.D., and the Cassini RADAR Team, 2008. A comprehensive backscatter map of Titan from the Cassini RADAR. Lunar Planet. Sci., Houston, TX. Abstract #2204.

Zebker, R.D., Wye, L.C., Janssen, M.A., and the Cassini RADAR Team, 2008. Titan's surface from reconciled Cassini microwave reflectivity and emissivity observations. Icarus 194, 704–710.